

Increased Occurrence and Intensity of Consecutive Rainfall Events in the China's Three Gorges Reservoir Area under Global Warming

Shuanglin Li¹, Yanxin Zheng², and Kalim Ullah³

¹Chinese Academy of Sciences

²China University of Geosciences

³COMSATS Institute of Information Technology

November 24, 2022

Abstract

Consecutive Rainfall Events (CREs) are important triggers of geological hazards like landslide downhill and mudslide in the Three Gorges Reservoir area (TGR), China. These hazards are not only potential risks for the effective storage capacity of the reservoir but also threats of the safety of the reservoir's Great Dam. The future changes of CREs' occurrence and intensity are analyzed by using the projection experiments from twenty models attending the Coupled Model Inter-comparison Project phase 5 (CMIP5) under three different representative concentration pathways (RCP2.6, RCP4.5 and RCP8.5). Spring and fall are focused on, during which CREs are most frequent. Considering a common overestimate of rainy days number in the state-of-the-art models, a new approach is developed to define CREs based on the percentile of rainfall distribution in observations. The approach yields a similar CREs climatology in models to that in observations, and thus is used to identify CREs in models. The results based on multiple model ensemble (MME) and model spread comparison suggest a significant increase in spring and an overall decrease in fall in CREs' occurrence under all three scenarios. As for the intensity, it is projected to intensify both in spring and fall. Particularly, the higher the emission scenario, the greater the spring accumulated rainfall amount during a single CRE. These results imply an increasing risk of geological hazards in the TGR in the future.

1 **Increased Occurrence and Intensity of Consecutive Rainfall Events**
2 **in the China's Three Gorges Reservoir Area under Global Warming**

3
4 Yanxin Zheng¹, Shuanglin Li^{2,3}, and Kalim Ullah⁴

- 5
6 1. Department of Atmospheric Science, China University of Geosciences, Wuhan 430074
7 2. Institute of Atmospheric Physics and Climate Change Research Center, Chinese Academy of
8 Sciences, Beijing 100029
9 3. College of Earth and Planetary Sciences, University of Chinese Academy of Sciences, Beijing
10 100049
11 4. Department of Meteorology, COMSATS Institute of Information Technology (CIIT), Islamabad,
12 Pakistan

13
14
15
16
17
18 To be submitted to earth and space science.

19
20
21 Corresponding author email: *shuanglin.li@mail.iap.ac.cn*
22
23
24
25
26
27
28

29

30

Abstract

31

32 Consecutive Rainfall Events (CREs) are important triggers of geological hazards
33 like landslide downhill and mudslide in the Three Gorges Reservoir area (TGR),
34 China. These hazards are not only potential risks for the effective storage capacity of
35 the reservoir but also threats of the safety of the reservoir's Great Dam. The future
36 changes of CREs' occurrence and intensity are analyzed by using the projection
37 experiments from twenty models attending the Coupled Model Inter-comparison
38 Project phase 5 (CMIP5) under three different representative concentration pathways
39 (RCP2.6, RCP4.5 and RCP8.5). Spring and fall are focused on, during which CREs
40 are most frequent. Considering a common overestimate of rainy days number in the
41 state-of-the-art models, a new approach is developed to define CREs based on the
42 percentile of rainfall distribution in observations. The approach yields a similar CREs
43 climatology in models to that in observations, and thus is used to identify CREs in
44 models. The results based on multiple model ensemble (MME) and model spread
45 comparison suggest a significant increase in spring and an overall decrease in fall in
46 CREs' occurrence under all three scenarios. As for the intensity, it is projected to
47 intensify both in spring and fall. Particularly, the higher the emission scenario, the
48 greater the spring accumulated rainfall amount during a single CRE. These results
49 imply an increasing risk of geological hazards in the TGR in the future.

50

51

52 **1. Introduction**

53 The Three Gorges Reservoir area (TGR), spanning 28-32°N latitudinally and
54 105-112°E longitudinally (see Figure 1), is a mountainous, highly populated region
55 locating in the middle reach of the Yangtze River basin, central China. It often suffers
56 from geological disasters like landslide and mudslide (Chen et al., 2012; Ma et al.,
57 2006). These disasters result in tremendous damages to the lives and properties. One
58 example is the landslide occurring in 1998, which caused a direct economic loss of
59 610 million RMB (Ma et al., 2005). In addition, they cause rockfall, mud and debris
60 flows, which block the rivers running to the reservoir, reduce the effective storage of
61 the reservoir (Zhang et al., 2016), even threaten the safety of the reservoir's Great
62 Dam. Therefore, predicting, warning and preventing geological hazards are an
63 important national demand in China.

64 Synoptic processes, especially Consecutive Rainfall Events (CREs), during
65 which it rains for one week and even longer with a gentle and moderate intensity, are
66 a substantial trigger to geological hazards, although other factors like short-duration
67 heavy rainfall or earthquake can be also important (Guzzetti et al., 2007; Ye et al.,
68 2009). Corominas and Moya (1999) illustrated that the risk of landslide increases
69 substantially when it rains persistently for several weeks with the moderate
70 accumulated rainfall amount over 200 mm. The size of the landslide may be
71 positively proportional to the duration of CREs (Jibson, 2006). One recent case is the
72 severe landslide occurring in Lishui (28.6°N, 119.9°E), Zhejiang Province on 13
73 November 2015, which resulted in 38 deaths (Liu, 2015). Prior to the landslide, it

74 rained lightly or moderately for nearly one month, with an intensity of only 6-8 mm
75 per day. No precursor was found and no warning was issued before the disaster. In
76 addition to trigger geological disasters, CREs adversely influence agricultural
77 production, cause local pooling or freezing rain during chilling weather, and affect
78 human health (Ding et al., 2008; Li et al., 1977; Sun et al., 2016). Therefore,
79 understanding the future trend of CREs is of substantial importance.

80 Previous analyses based on instrumental records suggest a decreasing trend in
81 spring CREs' occurrence, duration and accumulated rainfall amount, but an increase
82 in the mean daily rainfall during the past decades (Zheng et al., 2018; Zou, 2005). In
83 fall the trend is somewhat similar, with a decrease in occurrence despite an increase in
84 intensity (Sun et al., 2016; Wang and Zou, 2015). Whether such a trend persists into
85 the future is unclear.

86 Under the context of global warming, rainfall features change including its
87 occurrence frequency, duration, and intensity (Scoccimarro and Gualdi, 2013;
88 Trenberth, 1998; Zhai, 1999). Of particular importance is that rainfall becomes
89 regionalized and intensified, as far as one individual rainy event is concerned (Giorgi
90 et al., 2001; Lau et al., 2013; Sun et al., 2006). This inevitably leads to changes of
91 CREs. Thus, projecting the future trend of CREs in TGR consists of the preliminary
92 aim of the present study.

93 The reminder of this paper is organized as follows. Section 2 describes data and
94 methods. The projection experiments from the models attending the Coupled Model
95 Inter-comparison Project phase 5 (CMIP5) under three different representative

96 concentration pathways (RCP2.6, RCP 4.5 and RCP8.5) are used (Li et al., 2016;
97 Sillmann et al., 2013). Because of one common bias with too many rainy days in the
98 state-of-the-art models, the canonical method used to identify observational CREs
99 appears inappropriate for modeled precipitation. Thus a new approach is developed
100 for the models. Section 3 compares the CREs in the historical experiments with those
101 in observations. Since not all models reproduce the observed CREs well, just those
102 “good” models are selected to project the future trend. Section 4 gives the projection
103 results based on the multiple-model ensemble mean (MME) and an assessment of
104 result diversity in the individual models under different emission scenarios, with the
105 focus on the accumulated rainfall amount and daily rainfall intensity in CREs. Finally,
106 a summary and discussions are given in section 5.

107

108 **2. Datasets and methods**

109 *2.1 Datasets*

110 Gridded daily precipitation outputs from twenty models participating in CMIP5
111 are employed (Table 1). In order to treat all the models equally, only their first run
112 (r1i1p1) is analyzed. The experiments include the historical run with historically
113 evolving forcing for 1961-2005 and the projection runs with prescribed forcing of
114 RCP2.6, RCP4.5 and RCP8.5 for 2006-2099 (Taylor et al., 2012). RCP2.6 is a low,
115 peak-and-decay scenario in which radiative forcing reaches the maximum near the
116 middle of the 21st century before decreasing to an eventual nominal level of 2.6 W/m².
117 RCP4.5 is a medium stabilization scenario that follows a rising radiative forcing

118 pathway leading to 4.5 W/m^2 in 2100, while RCP8.5 is a high, business-as-usual
119 emissions scenario with radiative forcing increase to 8.5 W/m^2 by 2100. Details on
120 the CMIP5 models and their configurations are described at
121 <http://www-pcmdi.llnl.gov/>.

122 To assess the CMIP5 models' ability in reproducing the observed CREs, the daily
123 gauged grid precipitation dataset, referred to as CN05.1, is employed. CN05.1 was
124 produced by data from high-resolution stations across China during the period from
125 1961 to 2015. It uses thin-plate smoothing splines interpolation for climatology and
126 angular distance weighting interpolation for daily deviation before merging into the
127 full $0.25^\circ \times 0.25^\circ$ grids (Xu et al., 2009; Wu and Gao, 2013). This methodology
128 follows the method by which the CRU dataset was created (New et al. 2000). More
129 details about validation information of CN05.1 are given in Wu and Gao (2013). It has
130 been used by a lot of previous studies (e.g. Chen et al., 2014; Li et al., 2020; Pan et al.,
131 2020; Sui et al., 2015). In view of the possible mismatch in horizontal resolutions,
132 both the simulated precipitation and CN05.1 are re-gridded to a $1.0^\circ \times 1.0^\circ$ grid by
133 using a bilinear interpolation algorithm.

134

135 *2.2 Methods*

136 a) Definition of CREs

137 In observational studies (e.g. Li, et al., 1977; Zou, 2005), one CRE is isolated
138 when there are five or more consecutive rainy days. One rainy day is defined when
139 the accumulated amount is greater than or equal to 0.1 mm within 24 hours from

140 00UTC to the next 00UTC. For CN05.1, because of the rain intensity diffusion and
141 extended rainy days caused by interpolation, one elevated threshold, 1 mm per day, is
142 used to define rainy days. One similar threshold was used in previous studies ([Giorgi](#)
143 [et al., 2011](#); [Mohan and Rajeevan, 2017](#); [Salinger and Griffiths, 2001](#)). Here one CRE
144 is defined to begin if any one of the following four cases: (1) it has at least 5
145 consecutive rainy days; (2) it has 6 or 7 rainy days within 7 or 8 consecutive days,
146 despite no 5 consecutive rainy days; (3) it has 7 or 8 rainy days within 9 to 10
147 consecutive days but has at least one rainy day within any two consecutive days,
148 although it does not meet (1) or (2) above; (4) it has more than 9 rainy days but has at
149 least one rainy day within any two consecutive days, although it does not meet (1) (2)
150 and (3) above ([Sun et al., 2016](#); [Zheng et al., 2018](#)). The CRE termination is defined if
151 there are two consecutive non-rainy days following CRE, and the duration is the day
152 number from the beginning date until the ending date.

153 For the model outputs, the above definition is inappropriate because models
154 generally overestimate rainy day number but underestimate precipitation intensity
155 ([Dai and Trenberth, 2004](#); [Sun et al., 2007](#)). It will cause much-more-than-observed
156 CREs if a same 1 mm threshold is used. Previous studies developed various
157 calibration methods to correct the bias. The first one is the simplest unbiasing method
158 which simply overlaps the models' climatological mean bias into the simulations
159 ([Déqué, 2007](#)). It is straightforward, but has an implicit, unrealistic assumption that
160 the modeled mean rainfall follows the observed regardless of the variance. The second
161 is a combination of local intensity scaling with power transformation. It scales the

162 modeled precipitation within the observations, and corrects both the climatological
163 mean and variance (Fang et al., 2015; Schmidli et al., 2006; Teutschbein and Seibert,
164 2012). In details, modeled raw precipitation is calibrated by multiplying the ratio of
165 the observed mean precipitation to the modeled. The method will cause unmatched
166 successive days and weakened rainfall extremes. The third one is probability quantile
167 mapping (Semenov et al., 2010; Themeßl et al., 2012). It adjusts the climatological
168 mean, variance, and probability quantiles distribution of modeled precipitation and
169 has no influences on the extremes of the modeled rainfall. But it fails to correct the
170 temporal autocorrelation properties intrinsic to series, and neglects the physical
171 connection between variables (Boé et al., 2007). The fourth is the Artificial Neural
172 Networks (ANNs) technique. It efficiently handles the noisy and unstable data that are
173 typical in weather station observation, and maps highly nonlinear relationships
174 between a set of inputs and the corresponding outputs (Luk et al., 2000). The rainfall
175 estimates from ANNs are even more accurate than those based on statistical or
176 dynamic downscaling approaches (Mendes and Marengo, 2010; Skamarock et al.,
177 2008). But this technique is highly sensitive to the quantity and distance of
178 neighbouring gauges, and to the local hydrologic system as well (Hung et al., 2009).

179 In the present study, the long-term trend and future projection of CREs is
180 focused on, so the rainfall intensity in a single day is relatively less important than
181 whether it rains or not on that day. Since rainy day number may be subjective to
182 change in all the above calibration methods, we develop a new approach to defining
183 CREs instead. It is based on the Cumulative probability Distribution Function (CDF)

184 of daily rainy amount. The CDF in models is assumed to follow the observed, which
185 is calculated based on the threshold of 1.0 mm per day. Thus for the models the
186 threshold to define rainy days can be derived. Subsequently, rainy days number and
187 the CREs can be easily calculated at each grid points.

188

189 b) Variable to quantify CREs

190 A total of four variables are used to quantify the CREs, including occurrence
191 frequency (OCF), total rainy days (TRD), accumulated rainfall amount (ACR) and
192 mean daily rainfall intensity (INT). The first, OCF, describes the occurrence
193 climatology of CREs, while the latter three describe the duration and strength of one
194 single CRE. INT is not independent of ACR and TRD, but equal to ACR divided by
195 TRD. Previous studies suggest that all the four variables are linked to geological
196 hazards ([Corominas and Moya, 1999](#); [Jibson, 2006](#)), thus they are used for the present
197 analysis. Since CREs occur most frequently in spring and fall in TGR, just these two
198 seasons are focused on. Spring is referred to as 25 February to 4 June, while fall is
199 referred to as 28 August to 4 December considering the possibility that CRE
200 occurrence is not contained strictly in a whole calendar season.

201

202 c) Sen's slope estimate

203 Due to non-normal characteristics of probability distributions, trends of daily
204 precipitation amount and subsequently CREs cannot be estimated by the least squared
205 fitting. As [Santos and Fragoso \(2013\)](#) and [Mohan and Rajeevan \(2017\)](#), here the

206 trends are estimated by the Kendall's tau-based slop estimator (Sen's slope Q ; [Sen,](#)
207 [1968](#)) as follows

$$208 \quad Q = \text{median} \left(\frac{X_i - X_j}{t_i - t_j} \right) \quad (1).$$

209 Specially, for one time series with the length of L , at one time point (say t_i ,
210 $i=2, \dots, L$), slope can be calculated by using values (X_i) and (X_j) at time points t_i and t_j ,
211 respectively. Here t_j precedes t_i by at least one unit ($j=1, \dots, i-1$). As such, a total
212 number of $(L-1)!$ slopes can be obtained, and the median among all the slopes is the
213 best estimate of the trend. According to [Yue et al. \(2002\)](#), the Sen's slope is better than
214 the least squared fitting when estimating precipitation trend. Then, we use the least
215 squared fitting to estimate the intercept of the trend-dominated series ([Wang and](#)
216 [Swail, 2001](#)). Non-parametric Mann-Kendall test is used for significance validation,
217 since it is reliable for both monotonic linear and nonlinear trends in non-normal
218 distributed series ([Gotway, 1992](#)).

219

220 d) Metrics for model performance and selection

221 To assess model's ability in reproducing spatial pattern of CREs, the Taylor
222 Diagram ([Taylor, 2001](#)) is employed, which provides a statistical comparison of
223 simulated and observed CREs, in terms of spatial correlation coefficient,
224 root-mean-square (RMS) difference, and standard deviation. The RMS difference and
225 the standard deviation of various indices in the models are normalized by the
226 observed. Thus a perfect model has the RMS difference equal to 0, and the spatial
227 correlation and the ratio of spatial standard deviations both close to 1.

228 Because of no initialization for the oceanic model component in these CMIP5,
229 one should not expect that their historical runs have the ability to reproduce the
230 observed CREs evolution. Thus we compromise to assess their normalized temporal
231 standard deviation δ_m/δ_o (Han et al., 2014; Santer et al., 2009). Here δ_m and δ_o denote
232 the inter-annual standard deviation of model simulated and observed seasonal mean
233 CREs variables, respectively. The closer to 1 the value, the better the agreement
234 between simulation and observation is.

235 Considering the substantial importance of CRE occurrences, just OCF and TRD
236 are used to select “good” models. Three criteria are used based on Taylor diagram:
237 (1) the spatial correlation coefficient of models’ CRE occurrences with the observed is
238 above 0.31 (significant at the 95% level), (2) the normalized spatial RMS of CREs’
239 occurrences is less than 1.5, and (3) the normalized deviation of modeled spatial
240 CREs’ occurrences is smaller than 1.5 but great than 0.5. Besides, another more
241 criterion is considered: the normalized temporal standard deviation of simulated
242 occurrences is smaller than 1.5 but great than 0.5.

243

244 **3. Models’ simulation on CREs in the historical experiments**

245 The threshold for rainy days is derived before we evaluate the ability of the
246 models in reproducing the observed OCF and TRD. Figure 2 compares the CDFs
247 from the observations and the models. From it, the percentile with the cumulative
248 probability in the observed rainy days below the threshold (1.0 mm per day) is 60.49%
249 in spring (64.17% in fall) in all grid points. Correspondent to the same percentile, the

250 threshold is different from model to model. For example, for MRI-CGCM3 and
251 CSIRO-Mk3.6.0, the threshold is 2.1 mm per day in spring, 1.0 and 0.5 mm per day in
252 fall, respectively. The closer to 1.0 mm the derived threshold, the better the model is
253 in capturing the observed rainy days. A higher or lower threshold indicates an
254 overestimate or underestimate in modeled rainy days. Column 3 in table 2 gives the
255 derived threshold for the individual models.

256 After the threshold is derived, simulated CREs can be calculated subsequently.
257 Figure 3 is the Taylor diagram which compares the simulated and observed spatial
258 distribution of CREs. About one half of the models fail to reproduce the spatial
259 pattern of spring CREs, with the correlation less than 0.31. For fall, only a quarter of
260 the models exhibit a significant skill. MME of all twenty models (refer to as MME_A;
261 the character “A” means “all”, refer to Table 2 and Figure 3) shows a pronounced bias.
262 In spring, the spatial correlation coefficient in observed and MME_A OCF (TRD) is
263 0.74 (0.72), and the standard deviations in MME_A is underestimated relative to the
264 observed. In fall the modeled standardized deviations are close to the observed, but
265 the correlation coefficient is 0.38 (0.33) for the observed and model MME_A OCF
266 (TRD), even lower than that in spring.

267 By applying the criteria in section 2.2d, for spring a total of 11 models
268 (FGOALS-g2, IPSL-CM5A-LR, IPSL-CM5A-MR, CNRM-CM5, CanESM2,
269 HadGEM2-AO, HadGEM2-ES, MIROC5, MPI-ESM-LR, MRI-CGCM3,
270 CSIRO-Mk3.6.0) stand out as “good” models. For fall, a total of 5 models
271 (IPSL-CM5A-LR, IPSL-CM5A-MR, CNRM-CM5, MRI-CGCM3, CSIRO-Mk3.6.0)

272 are selected. MME of these “good” models (refer to as MME_G; the character “G”
273 mean “good” in Table 2 and Figure 3) exhibits an evident improvement in
274 reproducing the observed CREs, with the spatial correlation coefficient in the
275 observed and simulated OCF and TRD above 0.84 in spring (0.75 in fall) from these
276 “good” models. Also, the standardized deviations in these “good” models are closer to
277 the observed. Hereafter just the results from these “good” models are analyzed, and
278 for brevity MME is used to represent MME_G unless it is clarified specially.

279 Table 2 compares the performances of these “good” models along with their
280 MME and the observations. The seasonal mean accumulated rainfall amount (column
281 4) in observations in spring and fall is 328.1 and 250.3 mm, respectively, while this
282 value in models varies from 274 to 463 mm in spring (from 163 to 256 mm in fall).
283 The overall consistence in the models’ and the observed CREs climatology indicates a
284 qualitative reasonability of this derived threshold. The climatological OCF in
285 individual models and in MME is close to the observation (column 5) in both spring
286 and fall. As for trend, in spring, the OCF in observation (column 6) exhibits a
287 reduction, albeit a lack of significance. About a half of the models yield a same
288 negative trend as the observed, but no significant trend is seen in the models else. The
289 spring trend in MME is nearly neutral (0.01 times per decade), in contrast with a
290 reduction in observations (-0.10 times per decade). In fall the trend in models bears an
291 overall similarity to the observed, which is consistently negative among all the five
292 “good” models albeit being less significant. Also, their MME shows a significant
293 reduction, which is consistent with observations.

294 For TRD (column 7 and 8), the observed climatology is 18.1 and 18.6 days in
295 spring and fall, respectively. This value in most of the models is slightly greater both
296 in spring (from 18.4 to 20.5 days, except for MIROC in which it is 17.7 days) and fall
297 (from 21 to 25.2 days). As for trend, seven models among the eleven “good” for
298 spring and all the five “good” models for fall yield a reduction consistent with the
299 observed (column 8). Not surprisingly, MME yields a reduction both in spring and fall,
300 in agreement with a major of the models.

301 Above the models’ occurrence of CREs climatology and trends have been
302 analyzed. The interannual variability of CREs in these models is also compared with
303 the observations. Figure 4 (left panels to the black dashed vertical line) displays the
304 modeled and observed OCF and TRD evolutions. From it, the uncertainty (model
305 spread) within the models generally conforms to the observed, although the variability
306 is less evident. These analyses suggest that the occurrence of CREs in models is
307 overall comparable to the observed.

308 Based on OCF and TRD, the intensity of CREs (ACR and INT) is further
309 investigated. The observed ACR (column 9 and 10) is 143.1 and 148.6 mm in spring
310 and fall, respectively. The modeled value in spring is greater in most of models except
311 for IPSL (122.3 and 125.3 mm, respectively). Six models simulate a reduction trend,
312 consistent with the observation (-11.82 mm per 10 year). However, MME suggests an
313 increase trend. It may be not realistic, because it is dominated by CanESM2. In fall it
314 is less unanimous, with two models with a higher value and the three else with a
315 lower value. All five models and their MME show a reduction trend, consistent with

316 observation.

317 The observed INT (column 11) is 7.8 and 7.9 mm per day in spring and fall,
318 respectively. The value in spring in most of models (8.0 to 12.2 mm per day, except
319 for two IPSL models) is slightly greater, but somewhat smaller in fall (4.8 to 7.0 mm
320 per day). The observed INT trend exhibits negative in both the seasons. Only a small
321 fraction of models in spring (three out of eleven models) reproduces the observed
322 trend, but so do a major of models in fall (three out of five models) (column 12).
323 Figure 7 (left half to the vertical black dashed line) displays the modeled ACR and
324 INT evolutions in historical runs along with the observations. Although a comparison
325 of the evolutions itself does not yield much meaning due to no initialization as
326 mentioned in the above section, it can still provide insights into the interannual
327 variability. From it, the simulated inter-model spread conforms to the observed. These
328 analyses suggest an overall consistence of CREs in these selected models with the
329 observed. This lays a basis for projecting CREs' future change by using these "good"
330 models.

331

332 **4. Future projections of CREs**

333 *4.1 Occurrence*

334 Figure 4 (right to the black vertical dashed line) shows the projected occurrence
335 of CREs (OCF and TRD) averaged over TGR under three emission scenarios. In
336 spring (Figs. 4a and 4b), MME shows a significant increase in OCF and TRD under
337 all the three RCPs. The increase is most evident under RCP4.5. Most of the individual

338 models yield a consistent result with MME. For OFC, seven, eight and six models
339 among all the eleven models project the result consistent with MME under RCP2.6,
340 RCP4.5 and RCP8.5, respectively. The numbers are eight, eight and six for TRD.

341 In fall (Figs. 4c and 4d), a significantly reversed decrease trend is projected in
342 OFC and TRD. The higher the emission, the more obvious the decrease is. As for
343 individual models, for OFC, a total of three, three and five models among all the five
344 “good” models project a decrease under RCP2.6, RCP4.5 and RCP8.5, respectively.
345 The number is two, three and five for TRD.

346 In view of regional difference in CREs within TGR from south to north ([Zheng
347 et al., 2018](#)), whether the CREs trends vary in different subregions is intriguing.
348 Figure 5a shows the distribution of projected spring OFC and TRD trend in MME. A
349 resemblance is seen between them. First there is an overall increase in the whole
350 region, particularly its plain western section. Second, the increase is more visible
351 under the lower emissions (RCP2.6 and RCP4.5) than the higher emission (RCP8.5).
352 This has been seen in the area mean above.

353 Since the result from one single model may dominate MME, this causes
354 uncertainty of projected results. To assess the uncertainty, we analyze the agreement
355 of the models’ results. Figure 5b displays the spatial distribution of model number
356 projecting an increase in occurrence of CREs. From it, most of models show a
357 positive trend in OFC and TRD (warm yellow corresponds to an upward trend) in
358 spring. Also, more models are in agreement with MME in the western section. This
359 indicates a larger reliability in the CRE increase there (Fig. 5a).

360 The distribution of projected trend in occurrence MME in fall is displayed in
361 figure 6a. A decrease both in OFC and TRD is seen across the area, particularly over
362 the southwestern section. The decrease is even obvious under the higher emission
363 scenario. This is also seen from the distribution of the number of model (Fig. 6b). The
364 number of models is represented with deeper blue when they project an overall
365 downward trend in OFC and TRD (Figs. 4c and 4d). The southwestern section of
366 TGR projects a consistent decrease under all three scenarios, where CREs occur most
367 frequently in fall (Zou, 2005). Besides, the models' agreement increases along with
368 the enhancement of emissions. Almost all the five "good" models project a reduction
369 trend in occurrence across the region under RCP8.5, and the reduction in about one
370 half of the models is significant in these grid points.

371

372 4.2 Intensity

373 Strong precipitation increases the risk of geological hazards (Corominas and
374 Moya, 1999; Guzzetti et al., 2007; Jibson, 2006). Here we analyze the projected
375 intensity of CREs expressed as ACR and INT. From figure 7 (right to the vertical
376 black dashed line), a significant increase in ACR and INT in spring is seen under all
377 three RCP scenarios. The higher the emission, the more evident the increase is.
378 During 2070-2099, ACR is projects to increase by 19.4%, 29.2% and 30.8% under
379 RCP2.6, RCP4.5 and RCP8.5, respectively, relative to 1970-1999. The values for INT
380 are 11.9%, 16.6% and 25.7 %. Also, most of the model bear a consistent projection
381 with MME. The number of the models is nine, ten and eight for ACR under RCP2.6,

382 RCP4.5 and RCP8.5 respectively. This number is eight, eleven and eleven for INT,
383 respectively.

384 In fall (Figs. 7c and 7d), a negative trend in ACR is projected, being significant
385 under RCP4.5 and RCP8.5. There is (are) one, three and three model(s) among the
386 five “good” models projecting the result consistent with MME under RCP2.6, RCP4.5
387 and RCP8.5, respectively. That only one model bears a similar projection to MME
388 implies substantial uncertainty under RCP2.6. For INT, one opposite result is
389 projected, but it may be robust since four, three and five models among all the five
390 “good” models yield a result similar to MME.

391 Figure 8a shows the spatial distribution of projected spring ACR and INT trend
392 in MME. ACR under all three scenarios shows an increase from north to south, while
393 INT increases in different sections under different emissions. Under the lower
394 scenario, the increase is located in the highly-populated southwestern section, but in
395 the northeastern closer to the Great Dam under the higher emissions. The model’s
396 spread is checked in Figure 8b. For ACR, almost all models project a positive trend
397 under all the three scenarios, particularly in the southwestern section. A greater spatial
398 homogeneity is seen in INT under RCP4.5 and RCP8.5 than that under RCP2.6.

399 The spatial distribution of projected fall ACR and INT trend in MME is
400 displayed in Figure 9a. Similar to occurrence (Figure 6a), a decrease in ACR is
401 located in the southwestern area, and it is more pronounced under the higher scenario.
402 INT shows an increase in the western section under RCP2.6 and RCP8.5, but a
403 decrease across the area under RCP4.5. Similar to the previous analyses, the model

404 number projecting a same trend as MME is presented in figure 9b. From it, the
405 models' agreement is relatively higher in ACR under higher than lower emissions.

406 Both the accumulated amount and short-duration rainstorm intensity are crucial
407 triggering geological hazards ([Corominas and Moya, 1999](#); [Jibson, 2006](#)). Thus, an
408 in-depth analysis on ACR and INT in individual models is conducted below. Figure
409 10 shows the frequency distribution of spring ACR bins for different decades under
410 RCP 4.5. In spite of an in-between difference, most of the models yield a visible
411 increase in the future. For example, there is an increased frequency of heavy ACR
412 (exceeding 80 mm) during 2070 to 2099 in CNRM-CM5, HadGEM2-AO,
413 HadGEM2-ES and MRI-CGCM3. Also, the increase in spring under different
414 scenarios is similar to one another, but with a greater amplitude under RCP8.5 than
415 RCP2.6. In fall, the individual models project a regional non-unanimous result except
416 for CNRM-CM5, which projects increased grids with ACR exceeding 200 mm during
417 the late 21st century. There is no significant change in the two models from IPSL but
418 a slight decrease from the two models else.

419 The increase in evaporation resulted by warming is greater than the atmospheric
420 capacity in holding moisture, this imbalance implicates a decrease in light to moderate
421 precipitation events ([Sun, 2006](#); [Trenberth, 1998](#)). The light to moderate precipitation
422 events consist of a fraction of CREs. To obtain the projection of precipitation
423 intensity in CREs (i.e. INT) in the future, the 90th, 95th and 99th percentiles obtained
424 by aggregating daily rainfall intensity from all CREs are used to classify four major
425 categories: light rainy (LR), moderate rainy (MR), heavy rainy (HR), and extreme

426 rainy (ER) days. Figure 11 compares the projected change in the individual models in
427 2020-2049 (near-future) and 2070-2099 (far-future) relative to 1970-1999. In
428 far-future, for spring LR (Fig. 11b) there is about a half of the models projecting a
429 reduction but an increase by the remaining models. For spring MR, more models
430 project an increase with a higher model agreement. Also, almost all models project an
431 increased HR and ER, and this is particularly evident by HadGEM2-ES,
432 HadGEM2-AO, and MRI-CGCM3. Besides, the increase is most significant under
433 high emissions. In fall, for LR, MR and HR, most models project weakening in daily
434 rainfall intensity, and the weakening is most prominent under all three scenarios in
435 MRI-CGCM3. In contrast, all the models display an enhanced daily intensity in ER
436 under RCP 2.6 and RCP 8.5.

437 In near-future the projected changes (Fig. 11a) are qualitatively similar to the
438 far-future but weaker. This indicates a gradual increase in spring daily rainfall
439 intensity during CREs in the future (Fig. 7b). In fall an overall increase is projected
440 (Fig. 7d), although it is not so unanimous in different categories. This increase may be
441 attributed to the growth of ER events. This seems reasonable because the precipitable
442 water within the atmosphere increases under a warming context, and it is easier to
443 form bigger particles and rain drops.

444

445 **5. Summary and discussions**

446 The Three Gorges Reservoir area (TGR) in China suffers from geological
447 hazards like landslide downhill and mudslide. Consecutive rainfall event (CRE) is a

448 substantial trigger. In this study we used the IPCC CMIP5 outputs to project the future
449 trends of CREs' occurrence and intensity. Just the "good" models are chosen to
450 project based on their historical simulations on the observed CREs.

451 Considering the common systemic bias with more rainy days in most of the
452 state-of-the-art models, a new approach to defining model's rainy days has been
453 developed based on the Cumulative probability Distribution Function of the observed
454 daily rainfall amount. Then, models' rainy days number has been derived to identify
455 CREs. A total of eleven /five models have been selected as "good" models to project
456 the future trends for spring /fall. These models have exhibited a relatively higher skill
457 in reproducing observed CREs' spatial patterns and interannual variability of
458 occurrence.

459 The results suggest an increase of the occurrence of CREs in spring, being most
460 significant under RCP4.5, but a reduction in fall, being more evident under higher
461 scenarios. The projected change in occurrence is more prone in the southern and
462 western sections of the area. The projected change in accumulated rainfall amount is
463 similar to the occurrence in both seasons. In contrast to difference in occurrence
464 between the two seasons, the projected daily rainfall intensity in CREs increases
465 overall in both spring and fall. The projected increase in occurrence and/or
466 intensifying in daily rainfall intensity imply a higher risk of geological hazards in
467 TGR in future.

468 It has been well known that CREs occur under a more stable and
469 longitudinally-oriented circulation pattern dominated with blocking at mid-high

470 latitudes (Ding et al., 2008; Luo et al., 2013). In the recent decades, the Arctic warms
471 much faster than the mid-lower latitudes, the weakening of the north-south
472 temperature gradient causes a reduction in the atmospheric baroclinicity and
473 subsequently weakens the mid-litudinal westerly and a much broader meridional
474 meanders in mid-high latitudes (Liu et al., 2012; Outten and Esau, 2012). The change
475 might affect the atmospheric pattern pattern related to CREs. From figure 12, the
476 spring geopotential height has increased obviously in east Siberia but not in the Ural
477 region through 1960-2018. In fall, a prominent increase occurs in the Barents Sea
478 region. Such a difference in atmospheric circulation trend between the two seasons
479 may have contributed their opposite trend in CREs' occurrence.

480 Here just the statistical downscaling scheme based on GCM outputs is used. In
481 addition to the statistical downscaling, the dynamical downscaling with regional
482 climate models is also an effective approach. It bears more physical meaning.
483 Projecting the future trend of CREs in regional climate model like WRF consists of
484 our future work.

485 There exists some uncertainty in the present study. First, climate simulations
486 have larger uncertainty over mountainous areas like TGR than over plain basins
487 (Palazzi et al., 2013, 2015). Precipitation is much more poorly simulated than other
488 variables such as air temperature, due to its strong localization, relatively sparse
489 instrument samples as well as the weaker physical constraints (Allen and Ingram,
490 2002). Also, the observational gridded dataset used here, CN05.1, embraces
491 uncertainty due to the adapted interpolation. Besides, the coarse spatial resolution of

492 the CMIP5 models is also one major source of uncertainties ([Birkinshaw et al., 2017](#)).

493 Finally, just several models (IPSL-CM5A-LR, IPSL-CM5A-MR, CNRM-CM5,
494 MRI-CGCM3, CSIRO-Mk3.6.0) analyzed here incorporate the direct effects and the
495 first indirect effects of aerosols, this affects definitely the identification and projection
496 of CREs since aerosols are essential for precipitation frequency ([Jing et al., 2017](#)).

497 This is another source of uncertainty.

498

499 **Acknowledgments**

500 The data that support the findings of this study are listed below. Original station
501 gauged data of CN05.1 can be obtained at a Chinese website
502 http://data.cma.cn/data/cdcdetail/dataCode/SURF_CLI_CHN_MUL_DAY_V3.0.html
503 after registration, and relevant English information can be found at
504 http://data.cma.cn/en/?r=data/detail&dataCode=SURF_CLI_CHN_MUL_DAY_CES
505 [_V3.0.](#) CMIP5 model outputs are available at website
506 <https://esgf-node.llnl.gov/search/cmip5/>.

507

508

509

510

Appendix: Abbreviation in the context

511

Abbreviated Index	Full name
CREs	Consecutive Rainfall Events
TGR	The Three Gorges Reservoir area
RCP	Representative Concentration Pathways
MME	Multiple-model ensemble mean
OCF	Occurrence frequency
TRD	Total rainy days
ACR	Accumulated rainfall amount
INT	Mean rainfall intensity

512

513

514 **References**

- 515 Allen, M. R., & Ingram, W. J. (2002). Constraints on future changes in the
516 hydrological cycle. *Nature*, 419(6903), 228-232.
517 <https://doi.org/10.1038/nature01092>
- 518 Birkinshaw, S. J., Guerreiro, S. B., Nicholson, A., Liang, Q., & Fowler, H. J. (2017).
519 Climate change impacts on yangtze river discharge at the three gorges dam.
520 *Hydrology and Earth System Sciences*, 21(4), 1911-1927.
521 <https://doi.org/10.5194/hess-21-1911-2017>
- 522 Boé, J., Terray, L., Habets, F., & Martin E. (2007). Statistical and dynamical
523 downscaling of the seine basin climate for hydro-meteorological studies.
524 *International Journal of Climatology*, 27(12), 1643-1655.
525 <https://doi.org/10.1002/joc.1602>
- 526 Chen, G., Sha, W., Iwasaki, T., & Ueno, K. (2012). Diurnal variation of rainfall in the
527 Yangtze River Valley during the spring - summer transition from TRMM
528 measurements. *Journal of Geophysical Research Atmospheres*, 117, D06106.
529 <https://doi.org/10.1029/2011JD017056>
- 530 Chen, X., Xu, Y., Xu, C., & Yao, Y. (2014). Assessment of precipitation simulations
531 in China by CMIP5 multi-models. *Progressus Inquistitiones De Mutatione*
532 *Climatis*, 10(3). <https://doi.org/10.3969/j.issn.1673-1719.2014.03.011>
- 533 Corominas, J., & Moya, J. (1999). Reconstructing recent landslide activity in relation
534 to rainfall in the Llobregat River basin, Eastern Pyrenees, Spain. *Geomorphology*,
535 30(1-2), 79-93. [https://doi.org/10.1016/S0169-555X\(99\)00046-X](https://doi.org/10.1016/S0169-555X(99)00046-X)

536 Dai, A., & Trenberth, K. E. (2004). The diurnal cycle and its depiction in the
537 community climate system model. *Journal of Climate*, 17(5), 930-951.
538 [https://doi.org/10.1175/1520-0442\(2004\)017<0930:TDCAID>2.0.CO;2](https://doi.org/10.1175/1520-0442(2004)017<0930:TDCAID>2.0.CO;2)

539 Déqué, M. (2007). Frequency of precipitation and temperature extremes over France
540 in an anthropogenic scenario: model results and statistical correction according
541 to observed values. *Global and Planetary Change*, 57(1-2), 16-26.
542 <https://doi.org/10.1016/j.gloplacha.2006.11.030>.

543 Ding, Y., Wang, Z., Song, Y., & Zhang, J. (2008). The Unprecedented Freezing
544 Disaster in January 2008 in Southern China and Its Possible Association with the
545 Global Warming. *Journal of Meteorological Research*, 22(4), 538-558.

546 Fang, G., Yang, J., Chen, Y., & Zammit, C. (2015). Comparing bias correction
547 methods in downscaling meteorological variable for a hydrologic impact study in
548 an arid area in China. *Hydrology and Earth System Sciences*, 19, 2547-2559.
549 <https://doi.org/10.5194/hess-19-2547-2015>.

550 Giorgi, F., Coppola, E., Raffaele, F., Diro, G. T., Fuentes-Franco, R., Giuliani, G., &
551 Torma, C. (2011). Higher hydroclimatic intensity with global warming. *Journal*
552 *of Climate*, 24, 5309-5324. <https://doi.org/10.1175/2011JCLI3979.1>

553 Giorgi, F., Whetton, P. H., Jones, R. G., Christensen, J. H., Mearns, L. O., Hewitson
554 B., vonStorch, H., Francisco, R. & Jack, C. (2001). Emerging patterns of
555 simulated regional climatic changes for the 21st century due to anthropogenic
556 forcings. *Geophysical Research Letters*, 28(17), 3317-3320.
557 <https://doi.org/10.1029/2001GL013150>

558 Gotway, C. A. (1992). Statistical Methods in Water Resources. *Technometrics*, 36,
559 323-324, <https://doi.org/10.1080/00401706.1994.10485818>

560 Guzzetti, F., Peruccacci, S., Rossi, M., & Stark, C. P. (2007). Rainfall thresholds for
561 the initiation of landslides in Central and Southern Europe. *Meteorology and*
562 *Atmospheric Physics*, 98(3-4), 239-267.
563 <https://doi.org/10.1007/s00703-007-0262-7>

564 Han, L., Han, Z., & Li, S. (2014). Projection of heavy rainfall events in the middle
565 and lower reaches of the Yangtze River valley in the 21st century under different
566 representative concentration pathways. *Transactions of Atmospheric Sciences*,
567 37(5), 529-540. <https://doi.org/10.13878/j.cnki.dqkxxb.20130512001>

568 Hung, N., Babel, M. S., Weesakul, S., & Tripathi, N. K. (2009). Tripathi. An artificial
569 neural network model for rainfall forecasting in Bangkok, Thailand. *Hydrology*
570 *and Earth System Sciences*, 13, 1413-1425.

571 Jibson, R. W. (2006). The 2005 La Conchita, California, landslide. *Landslides*, 3(1),
572 73-78. <https://doi.org/10.1007/s10346-005-0011-2>

573 Jing, X., Suzuki, K., Guo, H., Goto, D., Ogura, T., Koshiro, T., & Mülmenstädt, J.
574 (2017). A Multimodel Study on Warm Precipitation Biases in Global Models
575 Compared to Satellite Observations. *Journal of Geophysical Research*
576 *Atmospheres*, 21, 806-824. <https://doi.org/10.1002/2017JD027310>

577 Lau, K. M., Wu, H., & Kim, K. M. (2013). A canonical response of precipitation
578 characteristics to global warming from CMIP5 models. *Geophysical Research*
579 *Letters*, 40, 3163-3169. <https://doi.org/10.1002/grl.50420>, 2013

580 Li, H., Chen, H., Sun, B., Wang, H., & Sun, J. (2020). A Detectable Anthropogenic
581 Shift Toward Intensified Summer Hot Drought Events Over Northeastern China.
582 *Earth and Space Science*, 7, e2019EA000836.
583 <https://doi.org/10.1029/2019EA000836>

584 Li, M., Pan, J. & Tian, S. (1977). Forecast Method of Continuous Low Temperature
585 and Rainy Weather in Spring, Beijing, Science Press.

586 Li, W., Jiang, Z., Xu, J., & Li, L. (2016). Extreme Precipitation Indices over China in
587 CMIP5 Models. Part II: Probabilistic Projection. *Journal of Climate*, 24,
588 8989-9004. <https://doi.org/10.1175/jcli-d-16-0377.1>

589 Liu, C. (2015). Landslide disaster in Lidong Village, Yaxi Town, Liandu District,
590 Lishui City, Zhejiang Province. *The Chinese Journal of Geological Hazard and*
591 *Control*, 4, 5-5.

592 Liu, J., Curry, J. A., Wang, H., Mirong, S., & Radley M. H. (2012). Impact of
593 declining Arctic sea ice on winter snowfall. *Proceedings of the National*
594 *Academy of Sciences*, 109(11), 4074-4079.
595 <https://doi.org/1073/pnas.1114910109>

596 Luk, K. C., Ball, J. E., Sharma, A. (2000). A study of optimal model lag and spatial
597 inputs to artificial neural network for rainfall forecasting. *Journal of Hydrology*,
598 227(1-4), 56-65. <https://doi.org/10.7522/j.issn.1000-0534.2013.00018>

599 Luo, X., Li, D., & Wang, H. (2013). New Evolution Features of Autumn Rainfall in
600 West China and Its Response to Atmospheric Circulation. *Plateau Meteorology*,
601 32(4), 1019-1031. <https://doi.org/10.7522/j.issn.1000-0534.2013.00018>

602 Ma, Z., Zhang, Q., Zhu, R., & Jiang, Z. 2005: The Basic Characters of Mountain
603 Disasters and Relationship between Landslide and Rainfall in the Area of
604 Three-Gorge Reservoir. *Journal of Catastrophology*, 23(3), 319-326.
605 <https://doi.org/10.3969/j.issn.1008-2786.2005.03.011>

606 Ma, Z., Zhu, R., & Zhang, Q. (2006). Numerical simulation of severe precipitation in
607 Three-gorge Reservoir area and its application to landslide forecast. *Journal of*
608 *Natural Disasters*, 19, 1044-1052.

609 Mendes, D., & Marengo, J. A. (2010). Temporal downscaling: a comparison between
610 artificial neural network and autocorrelation techniques over the Amazon Basin
611 in present and future climate change scenarios. *Theoretical and Applied*
612 *Climatology*, 100(3), 413-421. <https://doi.org/10.1007/s00704-009-0193-y>

613 Mohan, S. T., & Rajeevan, M. (2017). Past and future trends of Hydroclimatic
614 Intensity over the Indian Monsoon Region. *Journal of Geophysical Research*
615 *Atmospheres*, 122(2), 896-909. <https://doi.org/10.1002/2016JD025301>

616 New, M., Hulme, M., & Jones, P. (2000). Representing twentieth-century space-time
617 climate variability. part ii: development of 1901-96 monthly grids of terrestrial
618 surface climate. *Journal of Climate*, 13(13), 2217-2238.
619 [https://doi.org/10.1175/1520-0442\(2000\)013<2217:RTCSTC>2.0.CO;2](https://doi.org/10.1175/1520-0442(2000)013<2217:RTCSTC>2.0.CO;2)

620 Outten, S. D., & Esau, I. (2012). A link between Arctic sea ice and recent cooling
621 trends over Eurasia. *Climatic Change*, 110(3), 1069-1075.
622 <https://doi.org/10.1007/s10584-011-0334-z>

623 Palazzi, E., Hardenberg, J. V., & Provenzale, A. (2013). Precipitation in the

624 Hindu-Kush Karakoram Himalaya: Observations and future scenarios. *Journal of*
625 *Geophysical Research Atmospheres*, 118(1), 85-100,
626 <https://doi.org/10.1029/2012JD018697>

627 Palazzi, E., Hardenberg, J. V., Terzago, S., & Provenzale, A. (2015). Precipitation in
628 the Karakoram-Himalaya: a CMIP5 view. *Climate Dynamics*., 45(1-2), 21-45.
629 <https://doi.org/10.1007/s00382-014-2341-z>

630 Pan, X. D., Zhang, L., & Huang, C. L. (2020). Future climate projection in Northwest
631 China with RegCM4.6. *Earth and Space Science*, 7, e2019EA000819.
632 <https://doi.org/10.1029/2019EA000819>

633 Salinger, M. J., & Griffiths, G. M. (2001). Trends in New Zealand daily temperature
634 and rainfall extremes. *International Journal of Climatology*, 21(12), 1437-1452.
635 <https://doi.org/10.1002/joc.694>

636 Santer, B. D., Taylor, K. E., Gleckler, P. J., & Bonfils, C. (2009). Incorporating model
637 quality information in climate change detection and attribution studies.
638 *Proceedings of the National Academy of Sciences*, 106(35), 14778-14783.
639 <https://doi.org/10.1073/pnas.0901736106>

640 Santos, M., & Fragoso, M. (2013). Precipitation variability in Northern Portugal: Data
641 homogeneity assessment and trends in extreme precipitation indices.
642 *Atmospheric Research*, 131, 34-45.
643 <https://doi.org/10.1016/j.atmosres.2013.04.008>

644 Schmidli, J., Frei, C., & Vidale, P. L. (2006). Downscaling from GC precipitation: A
645 benchmark for dynamical and statistical downscaling methods. *International*

646 *Journal of Climatology*, 26(5), 679-689. <https://doi.org/10.1002/joc.1287>

647 Scoccimarro, E., & Gualdi, S. (2013). Heavy precipitation events in a warmer climate:
648 results from CMIP5 models. *Journal of Climate*, 26(20), 7902-7911.
649 <https://doi.org/10.1175/JCLI-D-12-00850.1>

650 Semenov, M. A., & Stratonovitch, P. (2010). Use of multi-model ensembles from
651 global climate models for assessment of climate change impacts. *Climate*
652 *Research*, 41(1), 1-14. <https://doi.org/10.3354/cr00836>

653 Sen, P. K. (1968). Estimates of the Regression Coefficient Based on Kendall's Tau.
654 *Publications of the American Statistical Association*, 63(324), 1379-1389.
655 <https://doi.org/10.1080/01621459.1968.10480934>

656 Sillmann, J., Kharin, V. V., Zwiers, F. W., & Zhang, X. (2013). Climate extremes
657 indices in the CMIP5 multimodel ensemble: Part 2: Future climate projections.
658 *Journal of Geophysical Research Atmospheres*, 118(6), 2473-2493.
659 <https://doi.org/10.1002/jgrd.50188>

660 Skamarock, W. C., Klemp, J. B., & Dudhia, J. (2008). A Description of the Advanced
661 Research WRF Version 3. Boulder, CO, USA, National Center for Atmospheric
662 Research Technical Note.

663 Sui, Y., Lang, X. & Jiang, D. (2015). Temperature and precipitation signals over
664 China with a 2°C global warming. *Climate Research*, 64(3), 227-242.
665 <https://doi.org/10.3354/cr01328>

666 Sun, Y., Solomon, S., Dai, A., & Portmann, R. W. (2006). How often does it rain?
667 *Journal of Climate*, 19(6), 916-934. <https://doi.org/10.1175/JCLI3672.1>

668 Sun, Y., Solomon, S., Dai, A., & Portmann, R. W. (2007). How Often Will It Rain?
669 *Journal of Climate*, 20, 4801-4818. <https://doi.org/10.1175/JCLI4263.1>

670 Sun, Z., Huang, Y. & Ni, D. (2016). Climate and circulation characteristics of
671 continuous autumn rain in China. *Transactions of Atmospheric Sciences*, 39(4),
672 480-489. <https://doi.org/10.13878/j.cnki.dqkxxb.20140413001>.

673 Taylor, K. E. (2001). Summarizing multiple aspects of model performance in a single
674 diagram. *Journal of Geophysical Research Atmospheres*, 106(D7), 7183-7192.
675 <https://doi.org/10.1029/2000JD900719>

676 Taylor, K. E., Stouffer, R. J., & Meehl, G. A. (2012). An Overview of CMIP5 and the
677 Experiment Design. *Bulletin of the American Meteorological Society*, 93(4),
678 485-498. <https://doi.org/10.1175/BAMS-D-11-00094.1>

679 Teutschbein, C., & Seibert, J. (2012). Bias correction of regional climate model
680 simulations for hydrological climate-change impact studies: Review and
681 evaluation of different methods. *Journal of Hydrology*, 456, 12-29.
682 <https://doi.org/10.1016/j.jhydro.2012.05.052>

683 Themeßl, M. J., Gobiet, A., & Heinrich, G., (2012). Empirical-statistical
684 downscaling and error correction of regional climate models and its impact on
685 the climate change signal. *Climatic Change*, 112(2), 449-468.
686 <https://doi.org/10.1007/s10584-011-0224-4>

687 Trenberth, K. E. (1998). Atmospheric Moisture Residence Times and Cycling:
688 Implications for Rainfall Rates and Climate Change. *Climatic Change*, 39(4),
689 667-694. <https://doi.org/10.1023/A:1005319109110>

690 Wang, R., & Zou, X. (2015). An analysis on the change characteristics of
691 consecutive rainfall in the middle and lower reaches of the Yangtze River.
692 *Resources and Environment in the Yangtze Basin*, 24(9), 1483-1490, doi:
693 10.11870/cjlyzyyhj201509007

694 Wang, X. L., & Swail, V. R. (2001). Changes of Extreme Wave Heights in Northern
695 Hemisphere Oceans and Related Atmospheric Circulation Regimes. *Journal of*
696 *Climate*, 14(10), 2204-2221.
697 [https://doi.org/10.1175/1520-0442\(2001\)014<2204:COEWHI>2.0.CO;2](https://doi.org/10.1175/1520-0442(2001)014<2204:COEWHI>2.0.CO;2)

698 Wu, J., & Gao, X. (2013). A gridded daily observation dataset over China region and
699 comparison with the other datasets. *Chinese Journal of Geophysics*, 56(4),
700 1102-1111. <https://doi.org/10.6038/cjg20130406>

701 Xu, Y., Gao, X., Shen, Y., & Xu, C. (2009). A daily temperature dataset over China
702 and its application in validating a RCM simulation. *Advances in Atmospheric*
703 *Sciences*, 26(4), 763-772. <https://doi.org/10.1007/s00376-009-9029-z>

704 Ye, D., Zhang, Q., Zou, X., & Chen, X. (2009). Changing trends of major
705 meteorological disasters in recent decades over gorges reservoirir area. *Resources*
706 *and Environment in the Yangtze Basin*, 18(3), 296-300.
707 <https://doi.org/10.3969/j.issn.1004-8227.2009.03.017>

708 Yue, S., Pilon, P., Phinney, B., & Cavadias, G. (2002). The influence of
709 autocorrelation on the ability to detect trend in hydrological series. *Hydrological*
710 *Processes*, 16(9), 1807-1829. <https://doi.org/10.1002/hyp.1095>

711 Zhai, P. (1999). Detection of trends in China's precipitation extremes. *Acta*

712 *Meteorologica Sinica*, 25(1), 5-8.

713 Zhang, J., Ying, K., Wang, J., & Liu, L. (2016). Evaluation of landslide susceptibility
714 for Wanzhou district of Three Gorges Reservoir. *Chinese Journal of Rock*
715 *Mechanics and Engineering*, 35, 20-20.
716 <https://doi.org/10.13722/j.cnki.jrme.2015.0318>

717 Zheng, Y., Li, S., & Zhang, C. (2018). Climatic trend analysis of consecutive rainfall
718 events over Three Gorges Reservoir Area in spring. *Torrential Rain and*
719 *Disasters*, 37, 1-6. <https://doi.org/10.3969/j.issn.1004-9045.2018.04.009>

720 Zou, X. (2005). An Analysis on the Climatic Characteristics of Consecutive Rainfall
721 in the Three Gorges Area. *Journal of Catastrophology*, 20, 84-89.
722 <https://doi.org/10.1360/biodiv.050028>

723

724 Table 1 Details of the 20 CMIP5 models

ID	Model name	Institute (Institute ID)	Lat×Lon(degrees)
1	BCC-CSM1.1	Beijing Climate Center, China Meteorological Administration (BCC)	~2.8×~2.8
2	BNU-ESM	College of Global Change and Earth System Science, Beijing Normal University (GCESS)	~2.8×~2.8
3	FGOALS-g2	Institute of Atmospheric Physics, Chinese Academy of Sciences (LASG-IAP)	~2.8×~2.8
4	IPSL-CM5A-LR	Institut Pierre Simon Laplace (IPSL)	~1.9×3.75
5	IPSL-CM5A-MR		~1.25×2.5
6	CNRM-CM5	Centre National de Recherches Meteorologiques-Centre Europeen de Recherche et Formation Avancees en Calcul Scientifique (CNRM- CERFACS)	~1.4×~1.4
7	CanESM2	Canadian Center for Climate Modelling and Analysis (CCCMA)	~2.8×~2.8
8	GFDL-CM3	NOAA Geophysical Fluid Dynamics Laboratory (NOAA GFDL)	~2×2.5
9	GFDL-ESM2G		~2×2.5
10	GFDL-ESM2M		~2×2.5
11	HadGEM2-AO	Met Office Hadley Centre (MOHC)	1.25×~1.9
12	HadGEM2-ES		1.25×~1.9
13	MIROC-ESM	National Institute for Environmental Studies,The University of Tokyo (MIROC)	~2.8×~2.8
14	MIROC-ESM-CHEM		~2.8×~2.8
15	MIROC5		~1.4×~1.4
16	MPI-ESM-LR	Max Planck Institute for Meteorology (MPI-M)	~1.9×~1.9
17	MPI-ESM-MR		~1.9×~1.9
18	MRI-CGCM3	Meteorological Research Institute (MRI)	~1.1×~1.1
19	NorESM1-M	Norwegian Climate Centre (NCC)	~1.9×2.5
20	CSIRO-Mk3.6.0	Commonwealth Scientific and Industrial Research Organization in collaboration with Queensland Climate Change Centre of Excellence (CSIRO-QCCCE)	~1.9×~1.9

725

726

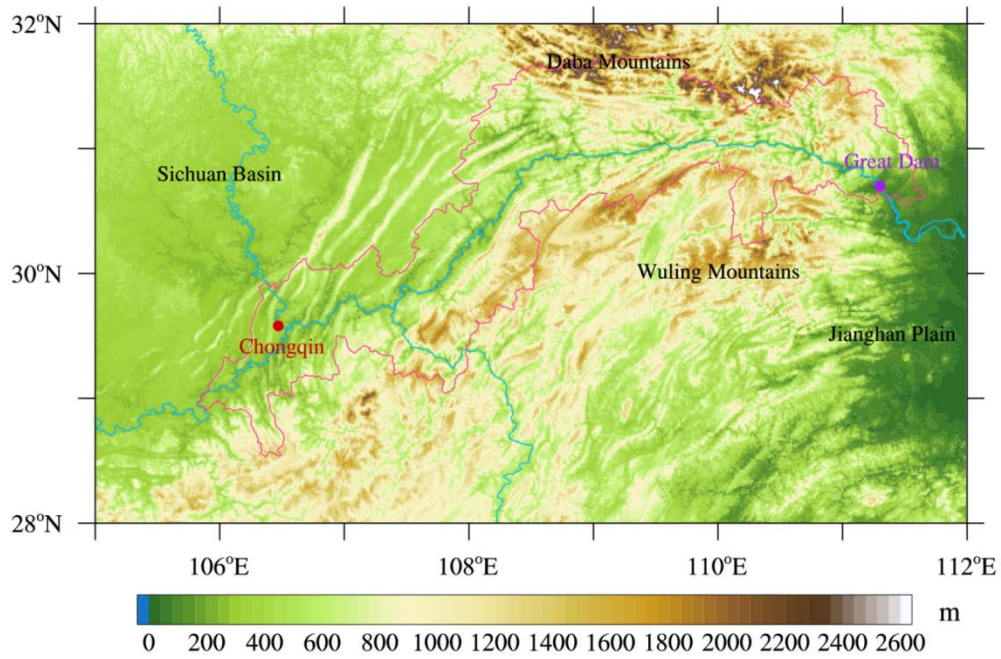
727

728 Table 2 One comparison of the threshold, modeled seasonal rainfall, averaged
729 magnitude and trend (per decade) of CREs in the historical runs of the “good” models
730 with those in observation. The four variables (OCF, TRD, ACR and INT) are used to
731 describe CREs, and CREs are identified by threshold based on the new approach. “ * ”
732 indicates significant at the 95% confidence level. See the context.

ID	Models	Spring									
		Thres.	Seasonal Rainfall	OCF		TRD		ACR		INT	
				Mag.	Trend	Mag.	Trend	Mag.	Trend	Mag.	Trend
	CN05.1	1	328.1	2.0	-0.10	18.1	-0.83	143.1	-11.82	7.8	-0.28*
3	FGOALS-g2	3.5	352.6	1.9	0.03	19.3	0.21	157.5	4.93	8.1	0.10
4	IPSL-CM5A-LR	1	276.2	2.1	0.01	18.9	-0.78	122.3	-3.42	6.5	0.05
5	IPSL-CM5A-MR	0.7	274.0	2.0	0.00	19.1	0.01	125.3	-1.37	6.6	-0.07
6	CNRM-CM5	3.1	379.4	2.0	-0.03	20.3	0.64	187.5	5.15	9.2	0.02
7	CanESM2	3	444.0	2.0	0.07	20.5	1.21	221.3	15.30	10.8	0.07
11	HadGEM2-AO	3.7	455.7	2.0	-0.02	18.9	-0.43	229.7	-5.61	12.2	-0.08
12	HadGEM2-ES	3.7	421.3	2.1	-0.09	18.4	-0.54	203.3	5.83	11.1	0.33*
15	MIROC5	3	462.8	2.0	-0.05	17.7	-0.68	192.5	-5.61	10.8	0.18
16	MPI-ESM-LR	3.2	454.8	2.0	0.05	18.4	0.02	195.9	5.12	10.6	0.38*
18	MRI-CGCM3	2.1	355.7	2.0	-0.09	19.9	-0.77	161.9	-8.65	8.0	-0.05
20	CSIRO-Mk3.6.0	2.1	375.0	2.0	-0.02	20.0	-0.08	176.9	-1.36	8.9	0.05
G	MME_G			2.0	0.01	19.2	-0.02	179.5	1.13	7.9	0.03
A	MME_A			2.1	0.00	19.7	-0.03	190.7	0.43	8.6	-0.02
		Fall									
		Thres.	Seasonal Rainfall	OCF		TRD		ACR		INT	
				Mag.	Trend	Mag.	Trend	Mag.	Trend	Mag.	Trend
	CN05.1	1	250.3	2.0	-0.24*	18.6	-2.90*	148.6	-27.42*	7.9	-0.18
4	IPSL-CM5A-LR	0.7	227.9	2.3	-0.20*	22.2	-1.92	155.8	-13.78	6.9	-0.10
5	IPSL-CM5A-MR	0.1	163.0	2.4	-0.16	25.2	-2.45	121.6	-14.2*	4.8	-0.04
6	CNRM-CM5	1.7	255.5	2.4	-0.04	22.0	-0.82	154.5	-2.73	7.0	0.06
18	MRI-CGCM3	1	239.2	2.2	-0.09	21.0	-1.19	137.5	-4.49	6.4	0.10
20	CSIRO-Mk3.6.0	0.5	190.4	2.3	-0.32*	22.1	-3.22*	129.6	-20.78*	5.7	-0.01
G	MME_G			2.3	-0.14*	22.5	-1.40*	139.8	-9.38*	5.8	-0.09
A	MME_A			2.2	-0.08*	21.9	-0.97*	167.8	-7.13*	7.0	-0.08

733

734



735

736 Figure 1 The topography distribution of the TGR. The west and east sections to TGR

737 are the Sichuan Basin and the Jiangnan Plain, and the north and south sections to TGR

738 are the Daba Mountains and the Wuling Mountains, respectively. The red dot of

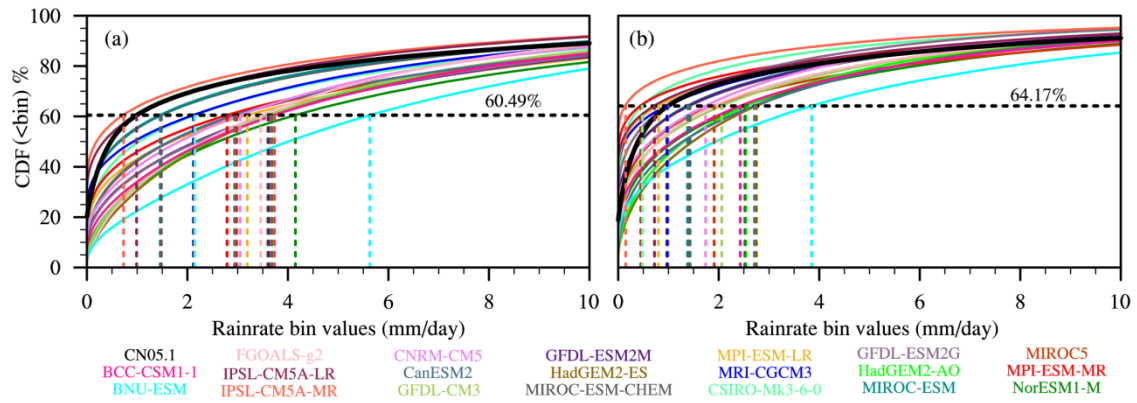
739 upstream is Chongqing City, which is a provincial capital with a population of 30

740 million, and the purple dot of the downstream indicates the location of the Great Dam

741 of TGR.

742

743



744

745 Figure 2 The CDF of daily rainfall amount in (a) spring and (b) fall based on CN05.1

746 and twenty CMIP5 models. The colorful curves represent different models and the

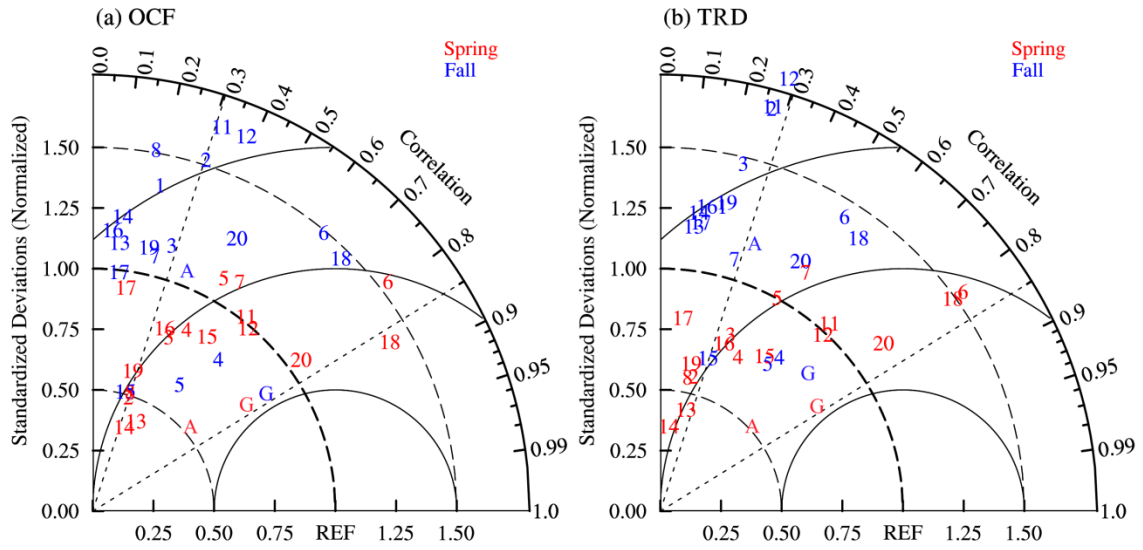
747 black curve represents the observation (CN05.1). The black horizontal dashed line

748 represents the CDF of observed daily rainfall with the amount over 1 mm threshold,

749 and the color vertical dashed lines correspond to the model threshold at horizontal

750 axis.

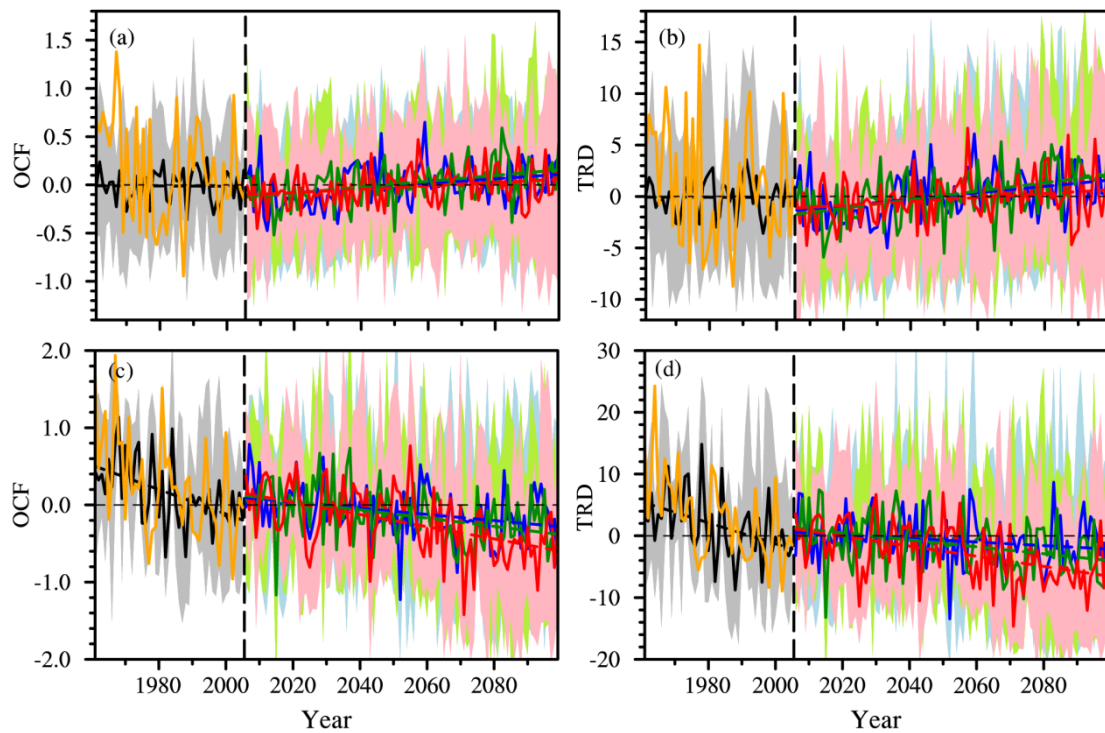
751



752

753 Figure 3 Taylor diagram displaying normalized pattern statistics of climatological
 754 seasonal mean (a) OCF and (b) TRD (models with a negative correlation coefficient,
 755 large root-mean-square difference or large standard deviation are not shown). Each
 756 number represents a model ID (see Table 1). The reference (REF) indicates
 757 observation from CN05.1. Red and blue denote the spring and fall, respectively. The
 758 correlation coefficient between a model and the CN05.1 is given by the azimuthal
 759 position, with oblique dotted lines showing the 95% confidence level. The normalized
 760 standard deviation of a model is the radial distance from the origin, with cambered
 761 thick dashed lines showing the value of 1.0 and cambered thin dashed lines showing
 762 the value of 0.5 and 1.5, respectively. The normalized centered RSM difference
 763 between a model and the reference is their distance apart, with cambered solid lines at
 764 intervals of 0.5.

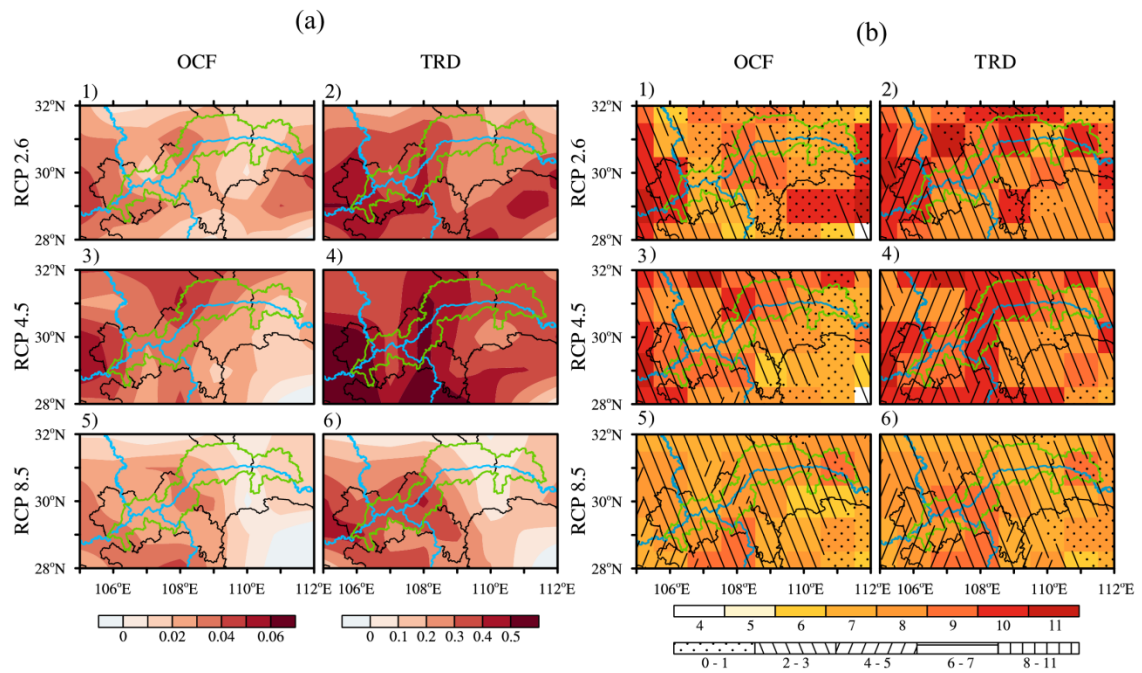
765



766

767 Figure 4 Temporal evolution of simulated OCF and TRD in spring ((a) and (b)) and
 768 fall ((c) and (d)) in CMIP5 historical runs (left to the vertical black line in each panel)
 769 and projected runs (right to the vertical black line). For the historical period
 770 (1961-2005), yellow and black lines represent the observed and MME simulated,
 771 respectively. For the projection period (2006-2099) blue, green and red lines represent
 772 three emission scenarios (RCP 2.6, RCP 4.5, RCP 8.5), respectively, with the
 773 correspondent linear fitting indicated with dashed lines. Shading with grey, light-blue,
 774 light-green and pink denotes the 95% confidence intervals of standard deviation for
 775 the “good” models in historical runs and projected runs (RCP 2.6, RCP 4.5, RCP 8.5,
 776 respectively). The anomalies are relative to 1961-2005.

777



778

779 Figure 5 a) Spatial change trend (per decade) of projected spring occurrence of CREs

780 from 2006 to 2099. b) Number of models among all the 11 models projecting a

781 positive trend of occurrence of CREs (warmer orange corresponding to a positive

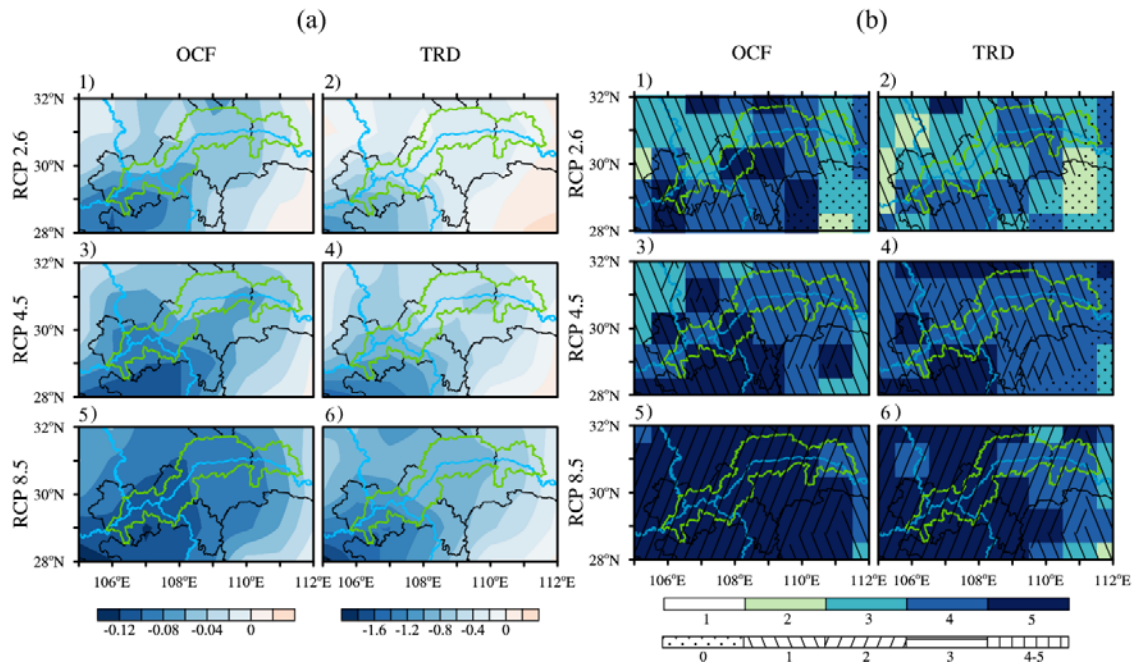
782 trend). Left to right correspond to the OCF and TRD describing occurrence of CREs,

783 and upper to lower corresponds to the three emission scenarios from RCP 2.6 to RCP

784 8.5. Colored shading in b) represents the number of models, and dots and hatches

785 shading indicate the number of models with significant trend.

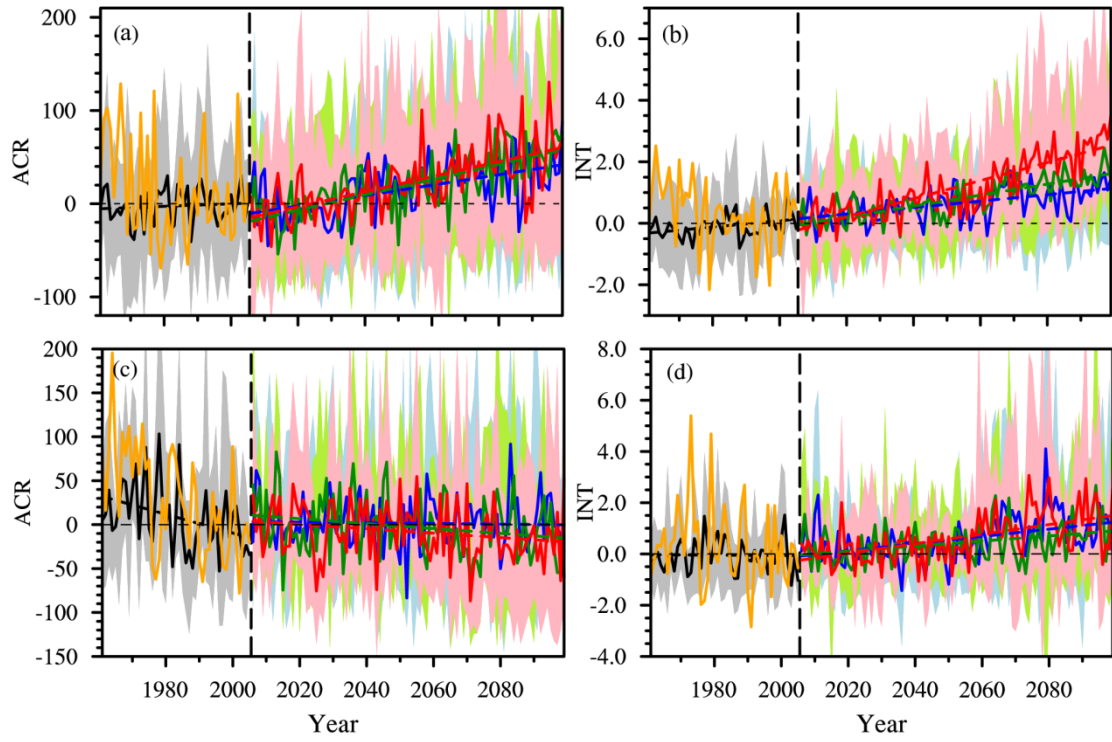
786



787

788 Figure 6 a) As Fig. 5a but for fall, and b) exhibits the number of models among all the
 789 5 models projecting a negative trend of occurrence of fall CREs (cooler blue
 790 corresponding to a negative trend).

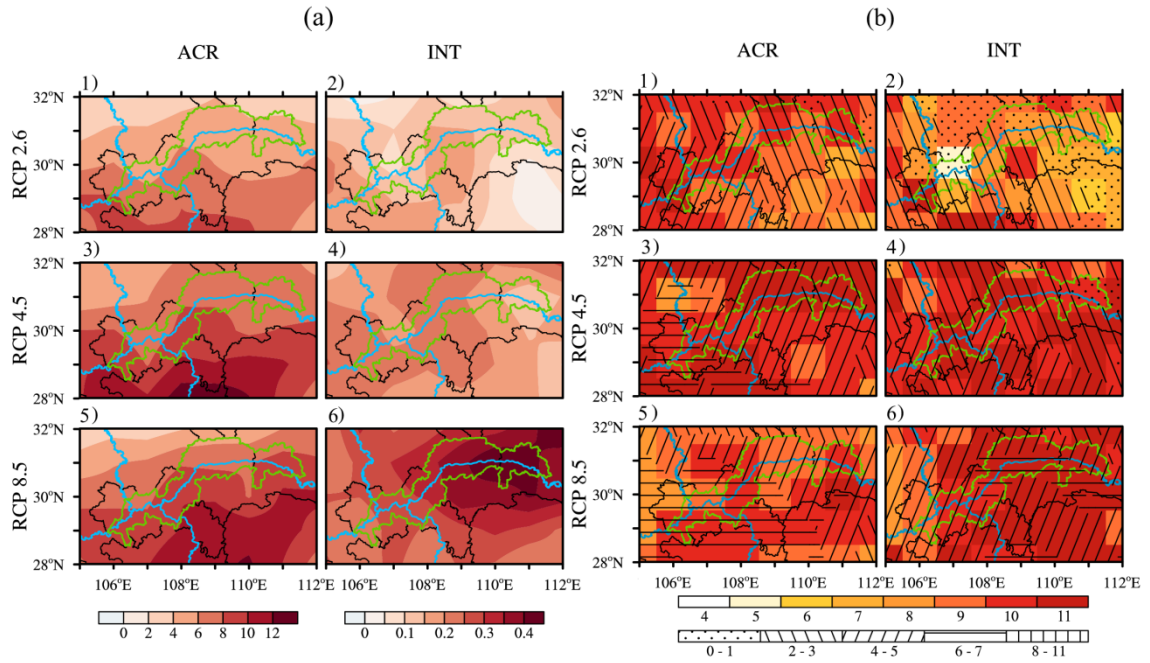
791



792

793 Figure 7 As Fig. 4 but for ACR and INT.

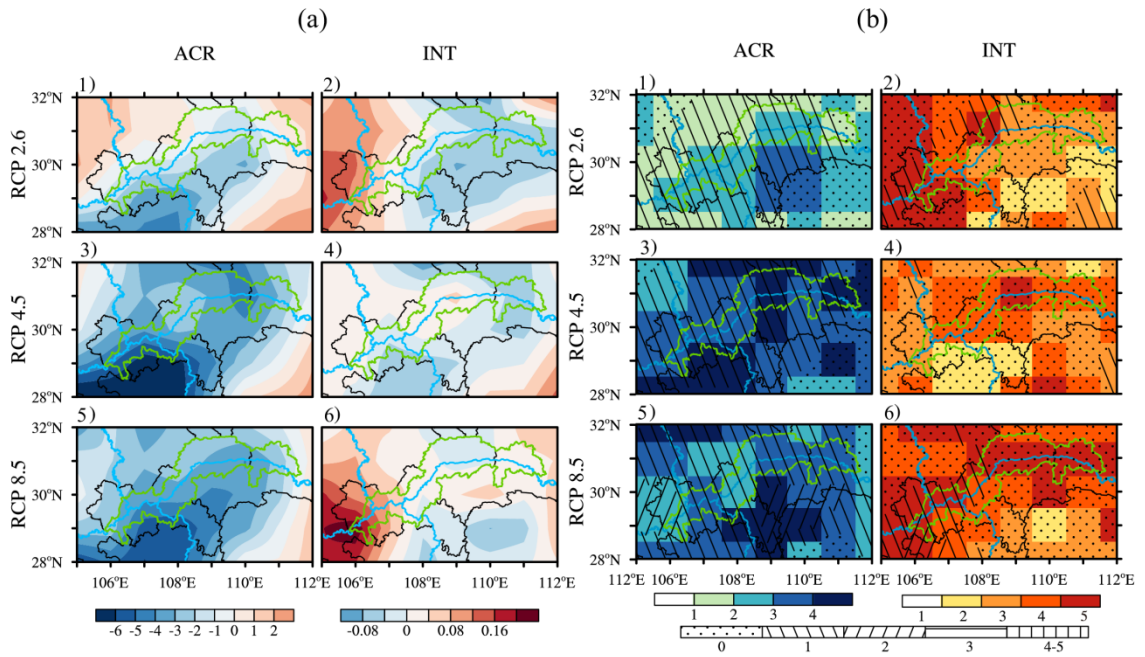
794



795

796 Figure 8 As Fig. 5 but for ACR and INT describing intensity of spring CREs.

797

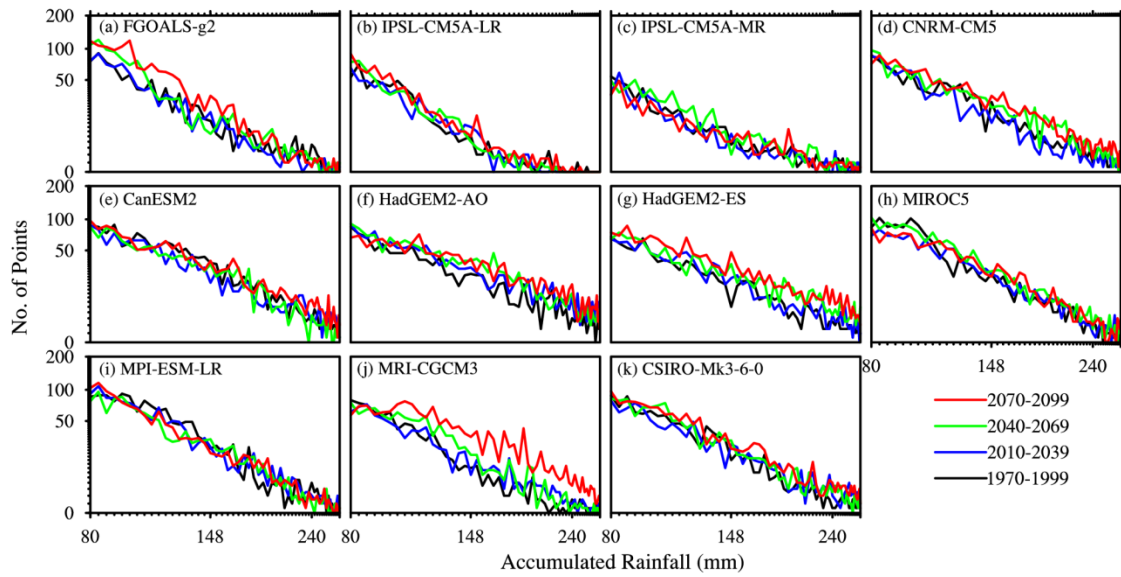


798

799 Figure 9 As Fig.6 but for ACR and INT describing intensity of fall CREs.

800

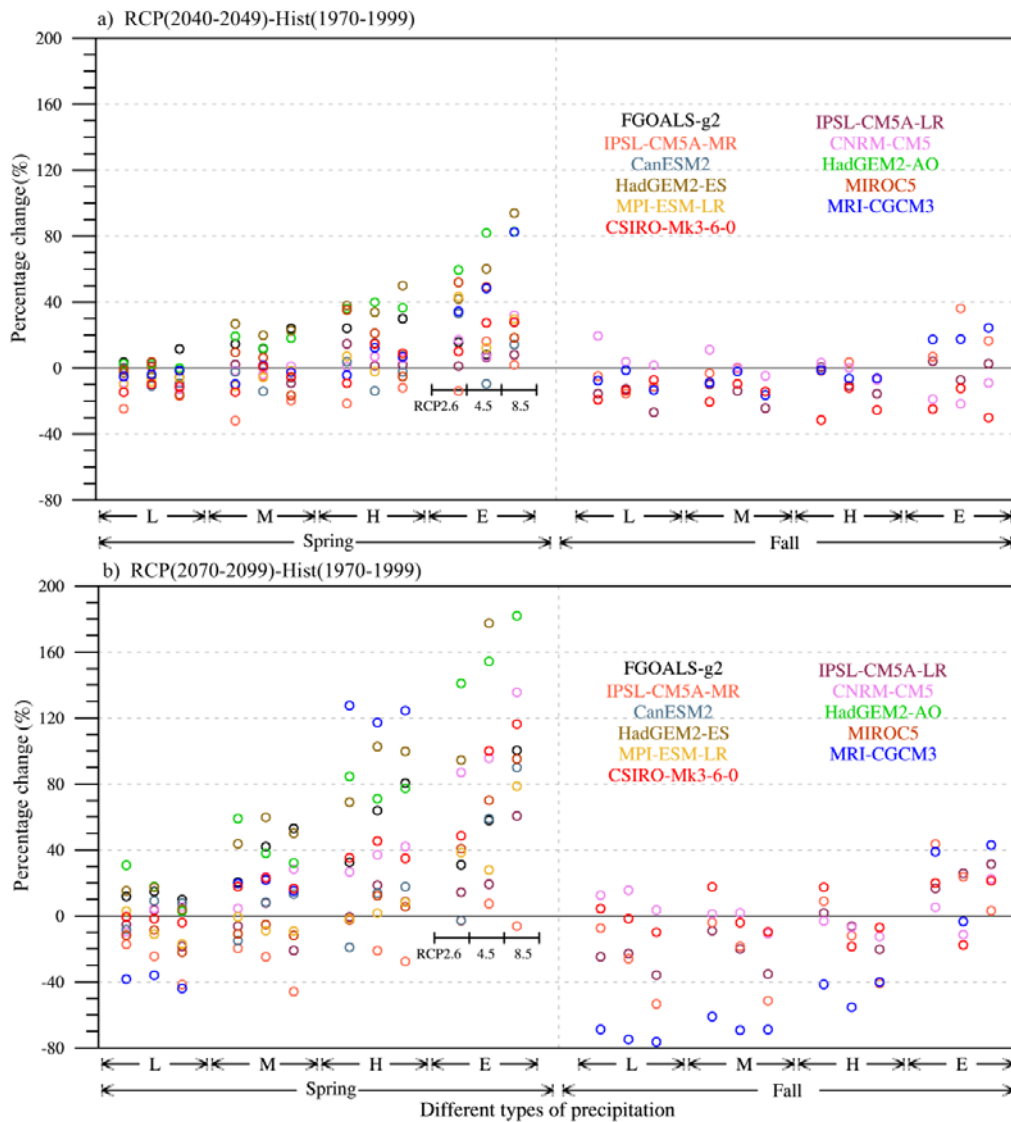
801



802

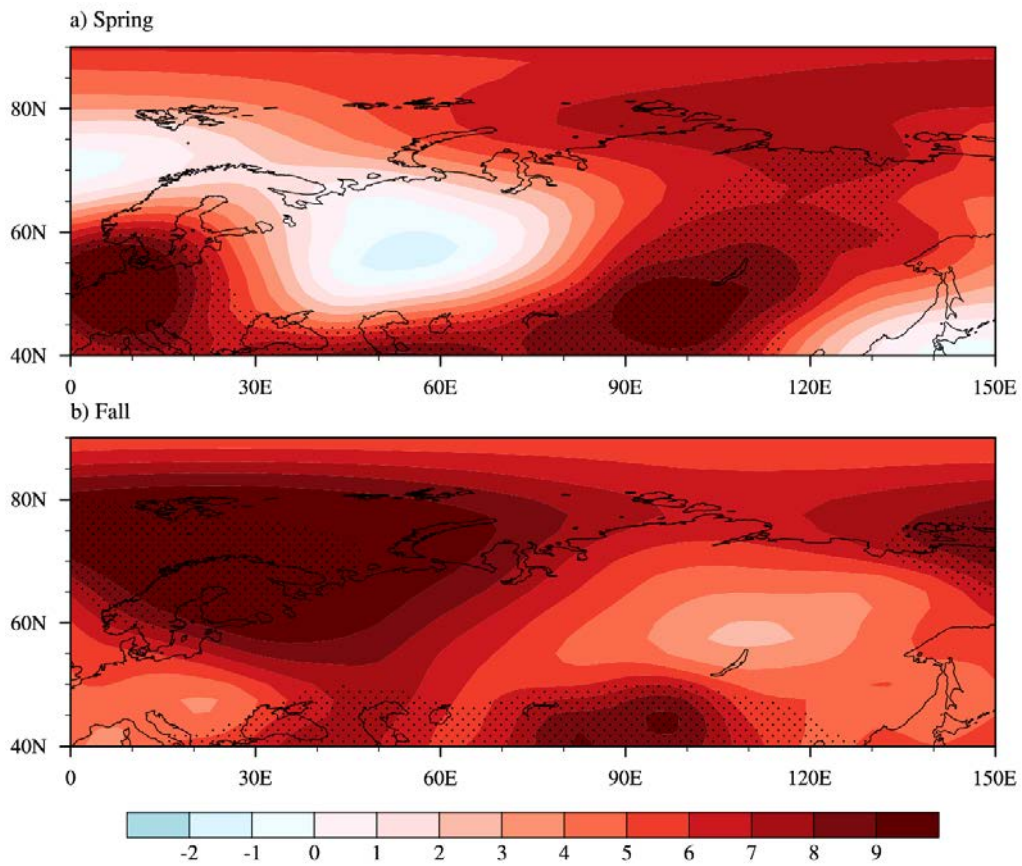
803 Figure 10 Frequency distribution of spring ACR in the single CRE for different
 804 rainfall bins during different decades of the future derived from “good” CMIP5
 805 models under RCP4.5.

806



807

808 Figure 11 The change rate of daily rainfall intensity at different categories during
 809 CREs. The increments are a) 2070-2099 or b) 2020-2049 relative to the reference
 810 period 1970-1999. Response of each “good” CMIP5 models is denoted by different
 811 color marks. Different categories of rainfall are shown as L(light rain), M(moderate
 812 rain), H(heavy rain), E(exterme rain). Part of models’ mark in b) (the ER growth of
 813 MRI-CGCM3 are 422%, 526%, 638% from RCP 2.6 to RCP 8.5 respectively, and the
 814 ER growth of HadGEM2-ES is the 235% under RCP 8.5) is not shown due to the
 815 oversized change rate.



816

817 Figure 12 Change trend of geopotential height at 500hPa level (units: m) in a) spring

818 and b) fall during 1960 - 2018 in the National Center for Environmental Prediction

819 reanalysis I. Regions within shaded in denote the trend or the differences at 99%

820 confidence level.

821

822